

# A 0.18- $\mu\text{m}$ CMOS Array Sensor for Integrated Time-Resolved Fluorescence Detection

Ta-chien D. Huang, *Student Member, IEEE*, Sebastian Sorgenfrei, Ping Gong, Rastislav Levicky, and Kenneth L. Shepard, *Fellow, IEEE*

**Abstract**—This paper describes the design of an active, integrated CMOS sensor array for fluorescence applications which enables time-gated, time-resolved fluorescence spectroscopy. The 64-by-64 array is sensitive to photon densities as low as  $8.8 \times 10^6$  photons/cm<sup>2</sup> with 64-point averaging and, through a differential pixel design, has a measured impulse response of better than 800 ps. Applications include both active microarrays and high-frame-rate imagers for fluorescence lifetime imaging microscopy.

**Index Terms**—Biosensor, CMOS image sensor, fluorescence, microarray.

## I. INTRODUCTION

**F**LUORESCENCE techniques find wide application in life sciences and are ideally suited for biomolecular detection both *in vivo* and *in vitro*. Targets molecules of interest, difficult to detect otherwise, are labeled with fluorophores. When optically excited, these fluorescent labels emit light at a longer wavelength than the excitation source. The difference in peak wavelengths between excitation and emission is referred to as the Stokes shift, typically 50 nm–100 nm. Precise optical filtering (of typically more than 160 dB) must be employed in almost all fluorescence applications for background rejection, filtering out the excitation light as shown in Fig. 1(a). Sensitive photodetection approaches, including cooled CCD imagers and photomultiplier tubes (PMTs), then measure the fluorescent signal.

One of the most pervasive *in vitro* applications of fluorescence is in surface-based biomolecular (DNA, protein) assays [1]. In this case, fluorescently-labeled analyte targets from solution bind to complementary probe molecules immobilized on a passive solid support. Confocal laser scanners are then employed to image these arrays. In traditional microarrays, issues of sensitivity, accuracy, specificity, and reproducibility limit the reliability of the platform. Fluorescent techniques are also widely employed *in vivo* to observe the location of labelled molecules [2]. Imaging systems in this case include both

wide-field epifluorescent microscopes and confocal laser-scanning microscopes.

Fluorophores have associated with them a characteristic lifetime, which defines the exponential fluorescent decay transient after the removal of the excitation source, as shown in Fig. 1(b). Fluorescent lifetimes are sensitive to excited-state reactions such as fluorescent resonant energy transfer (FRET) [4], enabling a growing field of fluorescent lifetime imaging microscopy (FLIM) [5]. The ability to time resolve fluorescent lifetimes on the same platform also enables detection of multiple fluorescent dyes simultaneously, similar to multi-color detection. Lifetimes, on the order of nanoseconds for organic dyes and longer for quantum dots [6], can be imaged spatially with detectors capable of fast time-gating. Such time-gated, time-resolved fluorescence detection also provides additional advantages in improved background rejection.

Time-resolved applications require a detector that is fast, as determined by the time-constant(s) of the impulse response, and sensitive, as determined by the minimum detectable integrated photon flux (photons/cm<sup>2</sup>). In most commercial time-resolved systems, time-correlated single photon counting (TCSPC) is employed with PMT detectors and laser scanning, with time resolution limited by jitter and sensitivity limited by dark count [7]. Frame rates are typically limited to fewer than 0.2 frames/s [8]. Alternate time-resolved fluorescence detectors rely on CCD imagers and gated intensifiers [9]. Frame rates of up to 100 frames/s have been achieved for a small imager (120-by-60) [10] if only two points of the decaying exponential are sampled, which is suitable for some monoexponential lifetime characterization.

Our previous effort [11] at a CMOS time-resolved imager was specifically directed toward active microarray applications. This imager had quantization-noise limited sensitivities of more than  $10^8$  photons/cm<sup>2</sup> and an impulse-response time constant of more than 1.1 ns, limited by a long “tail” in the photocurrent response of the diode. In this work, we consider the design of a time-resolved 64-by-64 CMOS imager specifically targeted for high-frame-rate FLIM applications [12], which improves on our earlier efforts in several significant ways. Differential photodiodes (PD) are implemented to improve photocurrent impulse response and noise immunity while preserving fast time gating. Thirteen-bit data conversion produces read-noise-limited sensitivities. Correlated double sampling (both digital and analog) reduces 1/f noise, and active reset is employed to reduce pixel reset noise. These combined techniques produce an imager with sensitivities approaching  $8.8 \times 10^6$  photons/cm<sup>2</sup>, a timing resolution of better than 150 ps, impulse-response time constants of better than 800 ps, and frame rates of better than 300 frames/s with two points per transient waveform.

Manuscript received August 08, 2008; revised December 30, 2008. Current version published May 01, 2009. This work was supported in part by Award Number R33HG003089 from the National Human Genome Research Institute, and in part by the National Science Foundation under Grant BES-428544, by NYSTAR, and by the C2S2 Focus Center Research Program.

T. D. Huang, S. Sorgenfrei, P. Gong, and K. L. Shepard are with the Columbia Bioelectronics Systems Laboratory, Department of Electrical Engineering, Columbia University, New York, NY 10027 USA (e-mail: tachien@cisl.columbia.edu; sorgenfrei@cisl.columbia.edu; gongping@cisl.columbia.edu; shepard@cisl.columbia.edu).

R. Levicky is with the Department of Chemical and Biological Engineering, Polytechnic University, Brooklyn, NY 11201 USA (e-mail: rlevicky@poly.edu).

Digital Object Identifier 10.1109/JSSC.2009.2016994

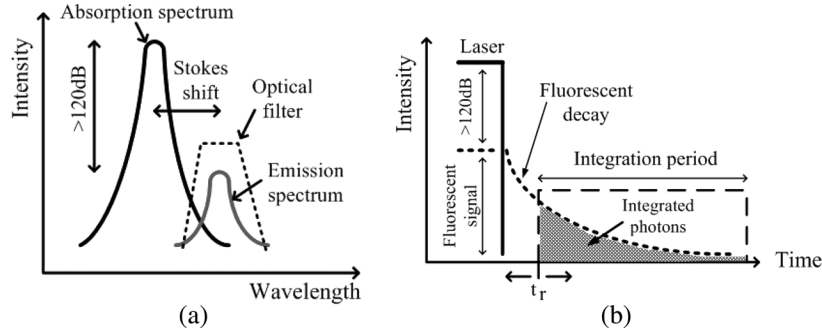


Fig. 1. Excitation/background rejection in fluorescence detection. (a) Optical filtering; (b) time-gating of excitation.

In Section II, we review the design issues associated with implementing a time-resolved imager based on a CMOS photodiode sensor. Section III describes design details of our time-resolved CMOS imager. A quantitative analysis of read noise is presented in Section IV. Section V presents measured characterization of the sensor and Section VI concludes.

## II. TIME-RESOLVED FLUORESCENCE DETECTION WITH CMOS ACTIVE PIXEL SENSORS

The issues in utilizing CMOS active pixel sensors (APS) for time-resolved fluorescence detection include impulse response, background rejection, sensitivity, and dynamic range.

### A. Impulse Response

A fast impulse response is a necessary attribute for any time-resolved detector. The measured time-resolved response of a fluorophore is the convolution of the fluorophore response with the detector impulse response

$$i_{det}(t) = \int_{-\infty}^{\infty} h_{det}(t - t') i_{fluor}(t') dt', \quad (1)$$

where  $h_{det}(t)$  is the impulse response of the detector and  $i_{fluor}(t)$  is the fluorophore's response to an ideal impulse excitation source. If the detector impulse response is significantly slower than the fluorophore response, this deconvolution cannot be done accurately. A slow detector impulse response also increases the requirement on optical filtering in order to achieve equivalent background rejection as described below.

### B. Background Rejection

Traditionally, fluorescence detection [13] requires external, dye-specific filters to achieve high SBR in non-time-resolved applications. Time-gated operation of the pixel, however, provides immediate enhancement to the signal-to-background ratio (SBR) without additional hardware. By gating the excitation source in the time domain and collecting only the photons emitted by the fluorescent dyes after the laser has been turned off, as shown in Fig. 1(b), it is possible to achieve a high SBR without external filters. The SBR in such time-gated operation can be written as

$$SBR = \frac{\int_{t_r}^{\infty} i_{signal}(t) dt}{\int_{t_r}^{\infty} i_{background}(t) dt} \quad (2)$$

where  $t_r$  denotes the start of the integration period after the excitation has been turned off, and  $i_{signal}(t)$  and  $i_{background}(t)$  are the resulting transient photocurrents due to the fluorescent signal and excitation background, respectively. Assuming the employed fluorophore exhibits an exponential decay that can be characterized by a single time constant,  $\tau_{fluor}$ , the fluorescent emission after the removal of the excitation can be generalized as

$$i_{signal}(t) = \Phi K_1 e^{-t/\tau_{fluor}} \quad (3)$$

where  $\Phi$  is the incident excitation light flux, and  $K_1$  is a fluorophore-specific coefficient which indicates the percentage of incident photons being absorbed and converted into fluorescent photons under the condition of constant incident photon flux. This coefficient is generally the product of the absorption cross section, quantum yield, and surface concentration of the fluorophores, as well as the photo collection efficiency and quantum efficiency of the photodetector. The characteristic lifetime can range from a few hundred picoseconds for organic fluorophores to several tens of nanosecond for quantum dots.

Assuming the detector impulse response exhibits a dominant time constant,  $\tau_{det}$ , that is much larger than the excitation turn-off time. The collected background signal can be written as

$$i_{background}(t) = \Phi K_2 e^{-t/\tau_{det}} \quad (4)$$

where coefficient  $K_2$  determines the percentage of the total charge, caused by the excitation, actually collected by the photodetector, discounting any reflection and both fluorescent and non-fluorescent absorption in the optical path.

The SBR can then be approximated by

$$SBR = \frac{K_1 \tau_{fluor}}{K_2 \tau_{det}} e^{-t_r \left( \frac{1}{\tau_{fluor}} - \frac{1}{\tau_{det}} \right)}. \quad (5)$$

$\tau_{det}$  must be much smaller than  $\tau_{fluor}$  in order to increase SBR. If a fluorophore with a short lifetime is used such that  $\tau_{det}$  approaches  $\tau_{fluor}$  in magnitude,  $t_r$  must be increased to delay the start of the integration period in order to increase SBR. Unfortunately, this causes the sensor to miss integrating the bulk of the total fluorescent signal, degrading the signal-to-noise ratio (SNR).

### C. Sensitivity

Most fluorescence systems relying on high-gain detectors such as photo-multiplier tubes (PMTs). In contrast, CMOS photodiodes have no inherent gain and must rely on low-noise amplification through an active pixel sensor (APS) design. In conventional CMOS imagers, long integration times [14] can be employed to increase SNR. In a time-resolved imager, however, a fixed transient photocurrent is available during each measurement cycle and averaging with multiple measurements must be employed to reduce temporal noise. For one measurement, the SNR is given by

$$SNR \approx \frac{\int_{t_r}^{\infty} i_{signal}(t)dt}{\sqrt{Q_{n,reset}^2 + Q_{n,readout}^2 + Q_{n,shot}^2}} \quad (6)$$

where  $\overline{Q_{n,reset}^2}$  is the input-referred reset noise sampled in each measurement,  $\overline{Q_{n,readout}^2}$  is the sum of input-referred noise from all circuits employed while reading the signal in the pixel, and  $\overline{Q_{n,shot}^2}$  is the input-referred photon shot noise. Averaging of  $N$  measurements increases the SNR by a factor of  $\sqrt{N}$ , and can in principle, be used to reduce the noise floor to quantization noise limits. In practice, frame-rate requirements generally require other approaches to noise reduction to limit the amount of averaging required.

### D. Dynamic Range

While sensitivity is the most important design metric for fluorescence imagers, dynamic range (DR) is a consideration. The upper bound of the system DR in conventional CMOS APS imager is often determined by pixel non-linearity before saturation. In a time-resolved measurement, the DR of the system can be extended by delaying the beginning of the integration window (increasing  $t_r$  as shown in Fig. 1(b)) such that the signal decays sufficiently to ensure non-saturation of the pixel. If the measured response is dominated by a single time constant, it is possible to extrapolate the time-resolved data back to the same initial time across different measurements independent of  $t_r$  extending the system DR.

## III. SYSTEM DESCRIPTION

The chip micrograph of the 5-mm-by-5-mm array sensor as fabricated in a standard mixed-signal 0.18- $\mu\text{m}$  process is shown in Fig. 2 [12]. The chip has 128 columns, each containing 32 active pixel sensors, one transimpedance amplifier (TIA), and one integrating analog-to-digital converter (ADC). These 128 columns are halved and end-abutted to form a square imager. Digital results from each ADC conversion are stored at the end of the conversion cycle, and each column decoder time-multiplexes and transmits stored data while the ADCs convert the next set of signals.

A programmable delay generator controls the arrival time of the reset signal relative to the laser pulse. An on-chip digital controller generates appropriate signals for the TIAs and ADCs and synchronizes the excitation source and gated integration. To avoid noise from the digital circuitry, the pixel circuitry, TIA and most of the ADC have a separate dedicated set of supply voltages. Double guard rings are also placed around the analog

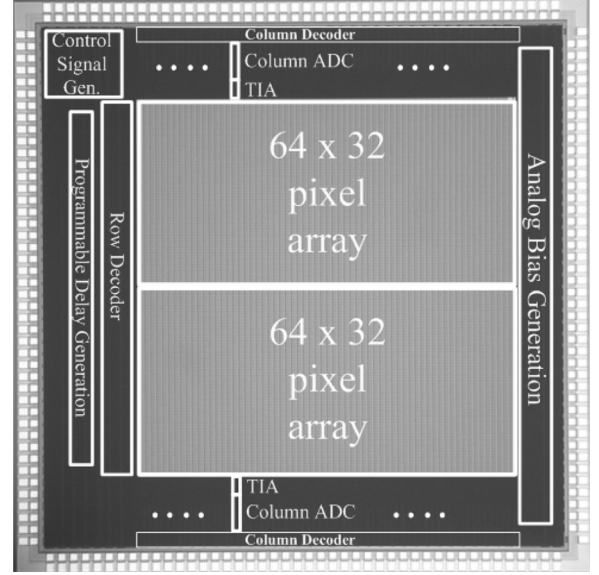


Fig. 2. Chip micrograph of the array sensor.

circuits and pixel array to mitigate the effects of substrate noise. All analog signals are routed through one side of the chip while digital signals are separated and routed on the other three sides. We now consider the design of the pixel, TIA, and ADC in more detail. Overall design specifications are summarized in Table I.

### A. Differential Pixel

Each pixel contains a differential photodiode (PD) and a differential transconductance amplifier which amplifies and transmits the integrated signal current-mode to the column TIA as shown in Fig. 3. Photocurrent  $i_{ph}$  collected within the integration period  $T_{int}$  appears as a differential voltage between node a and node b in Fig. 3, where  $V_b - V_a = i_{ph}T_{int}/C_{par}$ .  $C_{par}$  is the total capacitance at node a and node b, and is approximately 198.7 fF for this pixel design. Active reset-noise suppression is performed by the transconductor (M1a, M1b) through the negative feedback switch (M3a, M3b).

**Differential PD:** In this design, the photodiodes are implemented with n-well/p-substrate junctions to maximize the quantum efficiency in the optical range. The impulse response of the diode is determined by the convolution of the intrinsic photocurrent response and the RC time constant determined by the reset transistor and the diode capacitance, both of which must be made faster. Each pixel is 50- $\mu\text{m}$ -by-50- $\mu\text{m}$  with a total photodiode area of 576- $\mu\text{m}^2$ , leading to a fill factor of 23%.

For the pixel shown in Fig. 3, the equivalent RC time constant at the diode node during reset  $\tau_{D,reset}$ , as determined by the equivalent triode-region conductance ( $g_{d,M3a}$ ) of the reset devices (M3a, M3b) and the total capacitance at the diode node, is given by

$$\tau_{D,reset} = \frac{C_{par}}{g_{d,M3a}} \approx \frac{C_{PD} + C_{M1a,gate} + C_{M3a,drain}}{\mu_n C_{ox} \left(\frac{W}{L}\right)_{M3a} (V_{DD} - V_T)}, \quad (7)$$

where  $C_{PD}$  is the diode junction capacitance,  $C_{M1a,gate}$  is the gate capacitance of transistor M1, and  $C_{M3a,drain}$  is the drain capacitance of transistor M3. In this design the reset devices

TABLE I  
CHIP SPECIFICATIONS AND MEASURED PERFORMANCE

Item	Value
Technology	0.18 $\mu\text{m}$
Die size	5 mm x 5 mm
Pixel size	50 $\mu\text{m}$ x 50 $\mu\text{m}$
Array size	64 x 64
Active photodiode area	576 $\mu\text{m}^2$
Quantum efficiency (at 650nm)	0.42
Delay line resolution	150 ps
Signal path gain	$2 \times 10^{-6}$ DN/(photons/ $\text{cm}^2$ )
Sensitivity (with 64-point averaging)	$8.8 \times 10^6$ photons/ $\text{cm}^2$
Simulated pixel input-referred noise (with 64-point averaging)	23.4 $e^-$
Measured pixel input-referred noise (with 64-point averaging)	21.3 $e^-$
Simulated pixel impulse response time constant	860 ps
Measured pixel impulse response time constant	796 ps
ADC conversion time (single-ramp)	102 $\mu\text{s}$
ADC conversion time (dual-ramp)	1.6 $\mu\text{s}$
Frame rate (dual-ramp)	310 frames/s
Power Consumption	250 mW

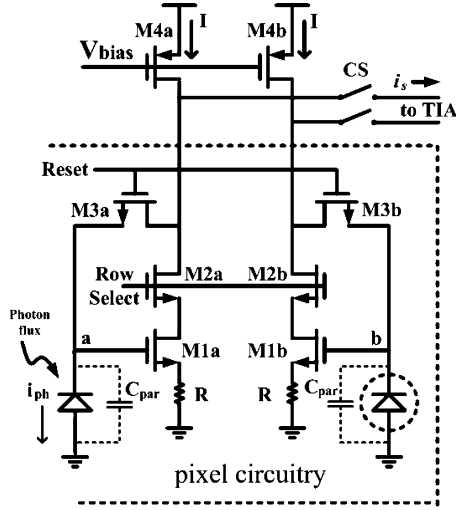


Fig. 3. Schematic of the differential pixel and column amplification.

have  $W/L = 1.08 \mu\text{m}/0.18 \mu\text{m}$  and  $\tau_{D,reset}$  is approximately 250 ps, making the diffusive component of the photocurrent impulse response the dominant factor in determining the overall pixel impulse response.

In conventional CMOS PDs, the photocurrent impulse response is determined by minority carriers generated within a diffusion length of the depletion region of the PD, which create a long “tail” as they diffuse and are collected. To attenuate this diffusive component, a fingered differential PD is used, as shown in Fig. 4(a), in which alternating fingers are covered with metal [15], rendering the diffusive component of the photocurrent common-mode. The size of these fingered pixels is limited by n-well spacing rules, with the number of fingers determined by common-mode rejection requirements. In this design, each pixel contains a total of eight PD fingers; each finger is 3.2  $\mu\text{m}$  wide and 45  $\mu\text{m}$  long. Finger periodicity, defined as the sum of finger width and spacing, is 4.8  $\mu\text{m}$ . For a given PD type and size, this common-mode rejection of the diffusive tail improves with increasing wavelength as the absorption depth increases. It can also be expected to improve with technology scaling as minimum n-well spacing

decreases. Fig. 4(b) shows the simulated photocurrent response of the covered and uncovered diode. The resulting differential impulse response is also shown. The impulse response time constant of the differential diodes, or  $\tau_{det}$  in (5), is expected to be approximately 860 ps from these simulations, compared with over 9 ns for a single-ended diode.

**Active Reset:** Reset noise is usually the most dominant component of temporal noise in a typical CMOS APS [16]. However, it is possible to reduce reset noise,  $Q_{n,reset}^2$ , with an active reset [17] which in this design is implemented through a common-source amplifier (transistors M1a and M1b) that negatively feeds back to the PD during reset [18], [19]. This pixel circuit is similar to a current-mode sample-and-hold (S/H) circuit [20], the noise performance advantages of which [21] are similar to CMOS APS active reset implementations [17]–[19]. In order to suppress reset noise effectively, the bandwidth of the transconductance amplifier, formed by transistor M1 and resistor R, must be larger than the diode bandwidth,  $1/2\pi\tau_{D,reset}$  during reset. Since we seek  $G_{m,pixel}/C_{par} \gg 1/\tau_{D,reset}$ , where  $G_{m,pixel} = g_{m,M1}/g_{m,M1}R + 1$  and  $g_{m,M1}$  is the transconductance of transistor M1 during reset, this leads to the requirement that  $G_{m,pixel} \gg g_{d,M3a} = 0.8 \text{ mS}$ .

**Differential Transconductor:** The pixel transconductors, which implement the active reset also perform differential voltage-to-current conversion with gain  $G_{m,pixel}$  for the pixel during integration. Nonsilicided polysilicon resistors are added to linearize the transconductor through source degeneration. The differential current signal from the transconductor is routed to the column-wise TIA. For intensity measurements, correlated double sampling (CDS), as described below, is used to mitigate the fixed pattern noise (FPN) that results from mismatch. In time-resolved measurements, such offsets do not affect performance since time series results are numerically differentiated.

### B. Transimpedance Amplifier

The column TIA converts the differential current from the pixel into a voltage, with a resistance of  $R_{TIA} = 1/G_{m,OTA}$  for subsequent column-level data conversion, where  $G_{m,OTA}$  is

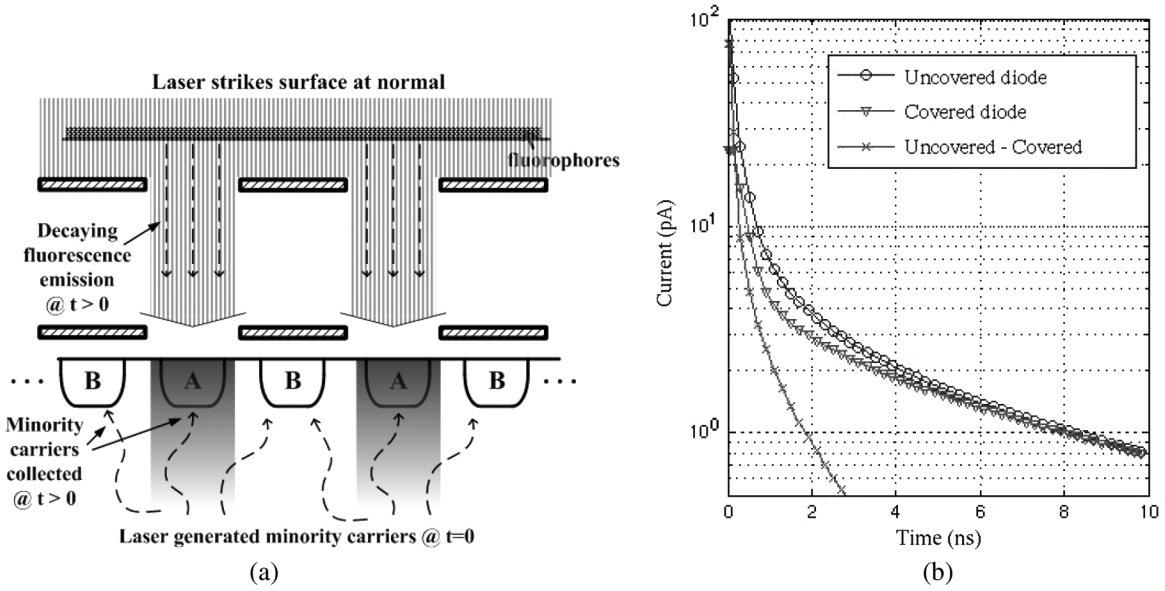


Fig. 4. Differential PD. (a) Operation of differential PD; (b) simulated photocurrent response of the differential PD.

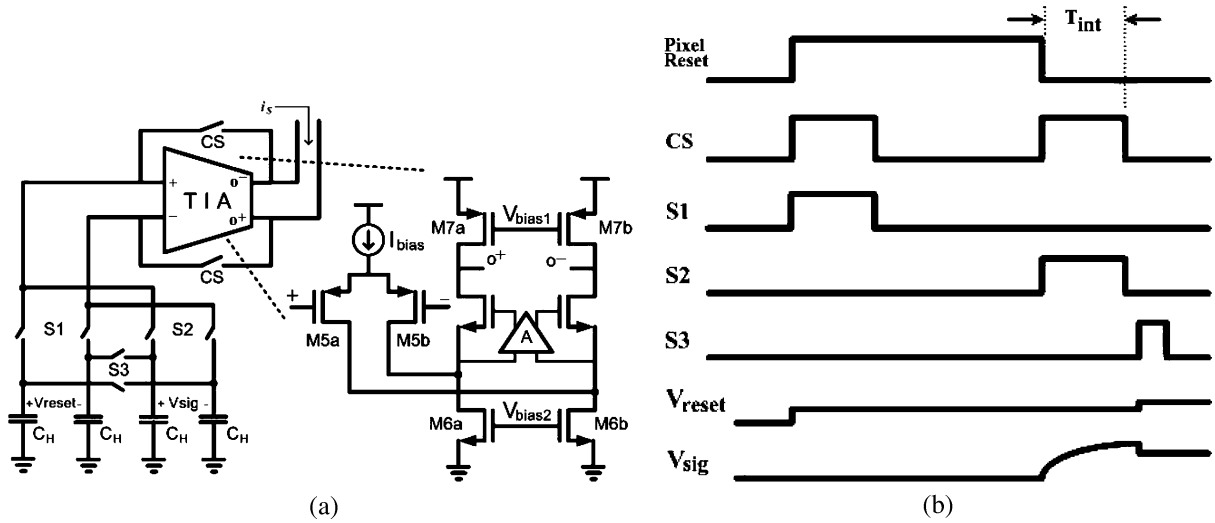


Fig. 5. Circuits and operations of CDS. (a) Switch capacitors for CDS; (b) waveform showing analog CDS operation.

the transconductance of the operational transconductance amplifier (OTA) shown in Fig. 5(a). Direct current-mode data conversion can also be configured, in which case the TIA is configured to operate as a current-mode sample-and-hold. The resistance  $R_{TIA}$  can be adjusted to provide an overall conversion gain of

$$A_{column} = G_{m,pixel} R_{TIA} \quad (8)$$

Large MOS capacitors  $C_H$  of 1 pF are used to hold the value of the converted differential voltage as shown in Fig. 5. The settling time at the holding capacitor  $R_{TIA} C_H$ , typically 1.2 ns, does not affect the detector impulse response as it is much shorter than typical integration times. Large capacitors  $C_H$  keep the temporal noise in the column circuits significantly below that of the pixel reset. Correlated double sampling (CDS) is implemented in both analog and digital forms with the circuits shown

in Fig. 5(a). To implement analog CDS, switched capacitors are used to store signals captured during reset ( $V_{reset}$ ) and after photocurrent integration ( $V_{sig}$ ) as shown in Fig. 5(b). The difference between these two signals is taken when switch S3 closes, after the second sampling period has completed, yielding a differential voltage equivalent to  $(1/2)(V_{sig} - V_{reset})$ . CDS can also be performed digitally, in which both samples are converted to digital values right after each of the integration periods and the difference taken digitally. In digital CDS, S1 and S2 are always on and S3 is always off such that sampling capacitance is twice that of analog CDS, lowering sampled kTC noise. Digital CDS works best for this system, allowing  $1/f$  to be reduced to the data converter quantization noise limit and exploiting the larger values for the sampling capacitors. Analog CDS could allow  $1/f$  noise to be reduced below these quantization noise limits, but this has no practical import in this case because of the integrated data conversion.

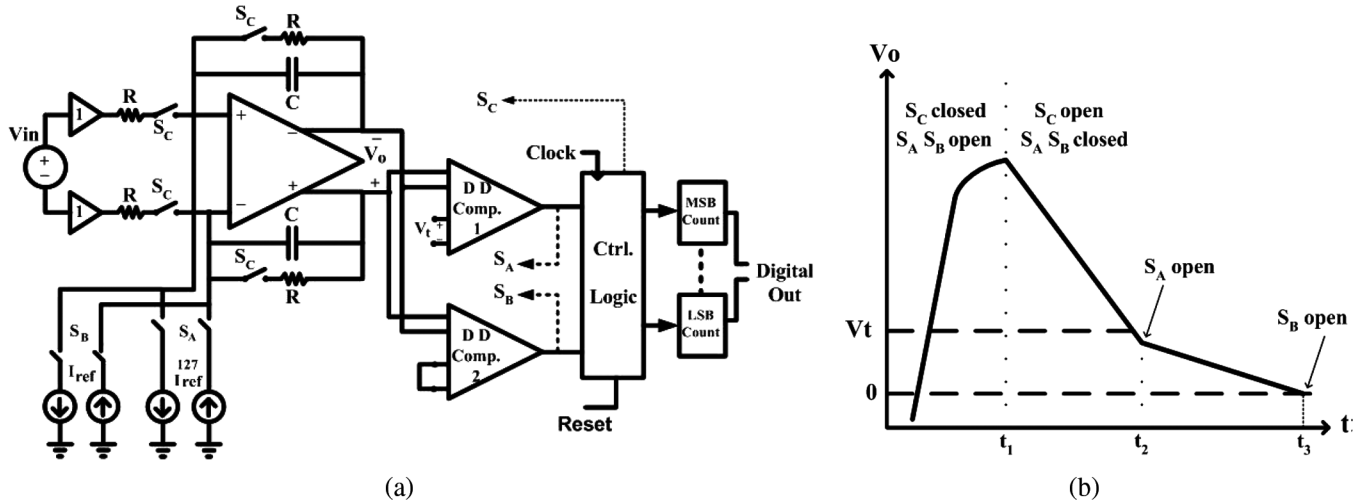


Fig. 6. Circuits and operations of ADC. (a) Schematic of dual-ramp integrating ADC; (b) waveform showing dual-ramp conversion.

### C. Analog-to-Digital Converter

A per-column integrating ADC is employed due to its relatively small area, low power, and high resolution. The conversion time of a conventional single-ramp, single-slope integrating ADC is limited by both ADC resolution and comparator speed. In our design, we seek a 13-bit resolution. We have a comparator capable of detecting a minimum (LSB) input voltage difference of  $24.4 \mu\text{V}$  in  $12.5 \text{ ns}$ . In a single-ramp architecture this results in a  $102 \mu\text{s}$  conversion time, which is insufficient for FLIM applications at video rate, where multiple conversions must also be performed for a single pixel in order to achieve noise-reducing objectives. In order to achieve at least 300 frames-per-second frame rates while allowing for 32-row-multiplexing, 64-point-averaging, and lifetime resolution of at least two points per transient, a differential dual-ramp, single-slope ADC architecture [22] is implemented as shown in Fig. 6(a). This dual-ramp ADC architecture delivers a conversion time of  $1.6 \mu\text{s}$ , 64-times faster than the single-ramp implementation using the same counter clock period,  $T_{clock}$ , requiring only an additional set of comparators and reference current sources. This exact speed up is given by one-half the ratio of coarse to fine reference currents, as described below.

Dual-ramp operation starts each conversion by closing switches  $S_C$  and opening switches  $S_A$  and  $S_B$ , sampling the input voltage at the output of the differential amplifier as shown in Fig. 6(b). At the start of the discharge/integration phase, the  $S_C$  switches are open while both  $S_A$  and  $S_B$  are closed, discharging the output with coarse current,  $128 \cdot I_{ref}$ . The differential voltage  $V_O$  decreases until it falls below the comparator threshold voltage  $V_t$ , at which time the top comparator in Fig. 6(a) signals the disconnection of switch  $S_A$  at the start of the next clock period. To utilize the counters efficiently,  $V_t$  is set to the voltage level discharged by  $128 I_{ref}$  in one clock period. Fine integration continues with fine reference current  $I_{ref}$  until the differential voltage at the output of the amplifier drops below zero. The most-significant-bit (MSB) counter stores the number of clock cycles required for coarse integration, as defined by the number of clock cycles between  $t_1$  and  $t_2$  in Fig. 6(b), while the least-significant-bit (LSB) counter

TABLE II  
SUMMARY OF CALCULATED READ NOISE WITHOUT AVERAGING

Item	Input-referred noise (rms)
Reset noise $\sqrt{Q_{n,reset}^2}$	$186.4 \text{ e}^-$
Pixel readout noise $\sqrt{Q_{n,readout}^2}$	$12.9 \text{ e}^-$
Quantization noise $\sqrt{Q_{n,quant}^2}$	$0.4 \text{ e}^-$
Total $\sqrt{Q_{n,reset}^2 + Q_{n,readout}^2 + Q_{n,quant}^2}$	$187.9 \text{ e}^-$

measures the number of cycles required for fine integration, defined by the time between  $t_2$  and  $t_3$ . Accuracy in the dual ramp operation is degraded by any mismatch between coarse and fine reference current sources. The ADC can operate as a single-ramp converter for better accuracy (but lower conversion rate) by combining both counters as a single counter and leaving  $S_A$  open during the entire integration phase. With a column conversion gain,  $A_{column}$  of eight and ADC fine reference current,  $I_{ref}$ , of  $0.74 \text{ nA}$ , the overall gain of the entire sensor path is approximately  $2 \times 10^{-6} \text{ DN}/(\text{photons}/\text{cm}^2)$ .

### IV. NOISE ANALYSIS

Although averaging can reduce overall temporal noise, a frame rate requirement of at least 300 frames/s in real-time FLIM applications limits the amount of averaging per frame to 64. Efforts must be made to reduce temporal noise to reduce averaging requirements. The dominant noise components include pixel reset noise, pixel transistor noise, TIA sample-and-hold noise, and the quantization noise of the ADC. Read noise sources are calculated below and summarized in Table II.

**Pixel Reset Noise:** With the use of active reset, the reset noise on  $C_{par}$  in Fig. 3 is reduced by a factor equal to  $G_{m,pixel}/g_{o,M3a}$  where  $g_{o,M3a}$  is  $0.8 \text{ mS}$ . The mean-squared noise voltage at the differential inputs of the pixel transistor due to reset is, therefore,

$$\overline{V_{n,reset}^2} = 2 \frac{g_{o,M3a}}{G_{m,pixel}} \cdot \frac{kT}{C_{par}} (= 2.3 \times 10^{-8} \text{ V}^2 \text{ at } 300 \text{ K}). \quad (9)$$

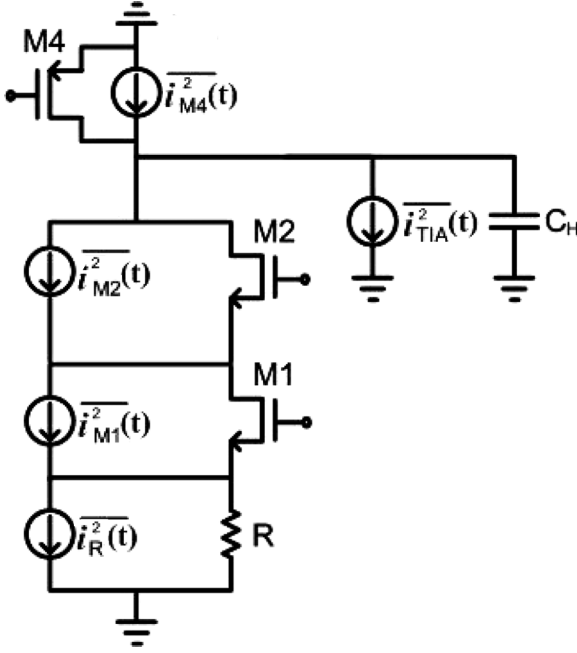


Fig. 7. Small-signal model for noise analysis during readout.

The reset noise at this node can also be expressed as the average noise charge

$$\overline{Q_{n,reset}^2} = C_{par}^2 \cdot \overline{V_{n,reset}^2} = 9.08 \times 10^{-34} C^2, \quad (10)$$

leading to an rms input-referred noise charge of 186.4 e<sup>-</sup> (see Table II).

**Pixel Transconductor and TIA Noise:** The pixel transconductor noise is dominated by the thermal noise of transistors M1a and M2a and the biasing device M4a shown in Fig. 3. The equivalent half-circuit model for noise analysis during signal amplification is shown in Fig. 7, in which  $i_R(t)$ ,  $i_{M1}(t)$ ,  $i_{M2}(t)$ ,  $i_{M4}(t)$  are thermal noise sources associated with each device in the pixel transconductor and  $i_{TIA}(t)$  represent the sum of all thermal noise sources in the OTA of Fig. 5(a) where  $\overline{i_{TIA}^2(t)}$  is defined as  $4 kT G_{m,OTA}^{noise}$  for comparison with noise sources from the pixel.  $1/f$  noise effects are rendered insignificant due to CDS and are excluded in this calculation. Assuming steady state operation, it can be shown that the constituent output-referred mean-squared differential noise voltages due to pixel readout are given by

$$\overline{V_{n,R}^2} = 2 \frac{kT}{C_H} \frac{1}{1 + \frac{1}{g_{d,M2}R} + \frac{1}{g_{m,M1}R}} \quad (11)$$

for source degeneration resistor R,

$$\overline{V_{n,M1}^2} = 2 \frac{2 kT}{3 C_H} \frac{1}{g_{m,M1}R + \frac{g_{m,M1}}{g_{d,M2}}} \quad (12)$$

for transistor M1a and M1b,

$$\overline{V_{n,M2}^2} = 2 \frac{kT}{C_H} \frac{1}{1 + \frac{g_{d,M2}}{g_{o,M1}}(1 + g_{m,M1}R)} \quad (13)$$

for transistor M2a and M2b,

$$\overline{V_{n,M4}^2} = 2 \frac{2 kT}{3 C_H} g_{m,M4} \left( \frac{1}{g_{d,M2}} + \frac{1}{g_{o,M1}}(1 + g_{m,M1}R) \right) \quad (14)$$

for transistor M4a and M4b,

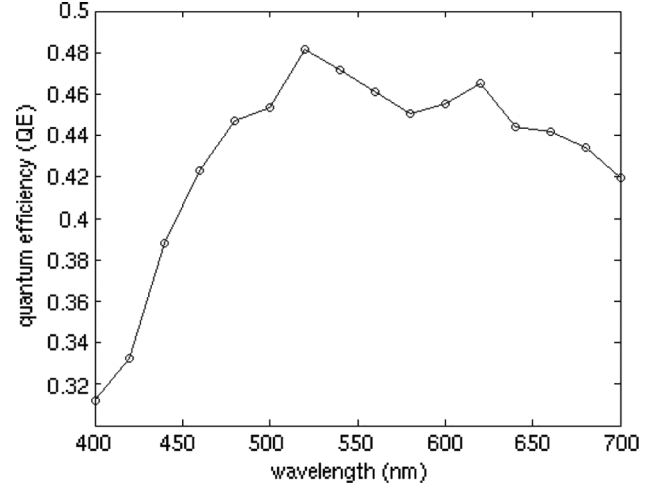


Fig. 8. Quantum efficiency of fingered n-well/p-sub photodiode sensor.

$$\overline{V_{n,TIA}^2} = 2 \frac{2 kT}{3 C_H} G_{m,OTA}^{noise} \left( \frac{1}{g_{d,M2}} + \frac{1}{g_{o,M1}}(1 + g_{m,M1}R) \right) \quad (15)$$

for TIA,

where  $g_{m,M1}$  and  $g_{o,M1}$  are the transconductance and output conductance of M1,  $g_{d,M2}$  is the channel conductance of M2, and  $g_{m,M4}$  is the transconductance of transistor M4 in Fig. 3.  $G_{m,OTA}^{noise}$  is given by

$$G_{m,OTA}^{noise} = g_{m,M5a,b} \left( 1 + \frac{g_{m,M6a,b}}{g_{m,M5a,b}} + \frac{g_{m,M7a,b}}{g_{m,M5a,b}} \right), \quad (16)$$

which includes the noise contributions of the transistors in the OTA as shown in Fig. 5(a) during readout. Since only one set of  $C_H$  capacitor is shared among the pixels in a column, they can be made much larger than  $C_{par}$ , suppressing the effect of pixel transconductor noise on overall read noise. If digital CDS is employed,  $C_H$  becomes  $2C_H$  in these expressions as the two holding capacitors are configured in parallel and the total input-referred mean-squared noise voltage from the pixel transconductor during readout is calculated to be

$$\overline{V_{n,readout}^2} = \frac{1}{A_{column}^2} \left( \overline{V_{n,R}^2} + \overline{V_{n,M1}^2} + \overline{V_{n,M2}^2} + \overline{V_{n,M4}^2} + \overline{V_{n,TIA}^2} \right) = 1.07 \times 10^{-10} V^2. \quad (17)$$

The total input-referred mean-squared noise charge is then

$$\overline{Q_{n,readout}^2} = C_{par}^2 \cdot \overline{V_{n,readout}^2} = 4.24 \times 10^{-36} C^2, \quad (18)$$

leading to an rms input-referred noise charge of 12.9 e<sup>-</sup> (see Table II).

**Quantization Noise:** Since we expect to employ averaging to reduce total temporal noise, the ADC must be able to set the LSB to be much lower than the calculated temporal noise in order to gain the benefits of averaging. The input-referred quantization step size at the pixel can be calculated as  $V_q = T_{clock} I_{ref} / C_H A_{column}$ . Assuming quantization error is

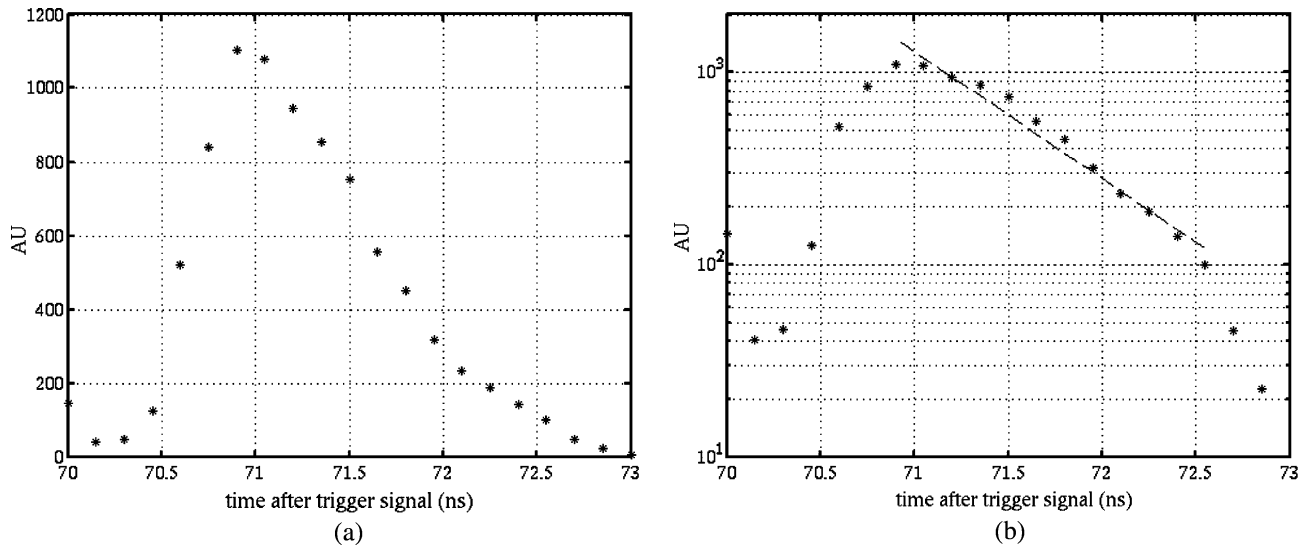


Fig. 9. Differentiated time-resolved detection of laser turn-off edge. (a) On linear scale; (b) on log scale.

not correlated, the input-referred mean-squared quantization noise voltage and charge are calculated as

$$\overline{V_{n,quant}^2} = \frac{V_q^2}{12} = 1.12 \times 10^{-13} V^2 \quad (19)$$

$$\overline{Q_{n,quant}^2} = C_{par}^2 \cdot \overline{V_{n,quant}^2} = 4.42 \times 10^{-39} C^2, \quad (20)$$

leading to an rms input-referred noise charge of  $0.4 e^-$  (see Table II) and allowing more than 240000 samples to be taken for averaging to reduce the dominant temporal noises before this quantization noise limit is reached.

## V. RESULTS

In this section, we present measured characteristics of the array sensor (summarized in Table I) as well as results using the array for time-resolved fluorescence detection.

### A. Array Characteristics

**Quantum Efficiency:** Fig. 8 shows the measured external quantum efficiency (QE) using a standard measurement setup including a monochromator, integrating sphere, and calibrated photodiode. Measured QE peaks just slightly above 40% for incident wavelengths between 600 nm and 650 nm.

**Time Domain Characterization:** Fig. 9 is the measured impulse response of the pixel. A PiLas Picosecond Laser Diode System with a 406-nm laser diode head is used for this measurement. This gain-switched laser is capable of producing laser pulses of less than 50-ps FWHM with peak collimated beam power as high as 150 mW. The laser pulses are synchronized with the chip. Results come from 4096-point averaging and numerically differentiating the resulting imager response. The data show that the system has an impulse response with a time constant of less than 800 ps. With fingered PD periodicity of  $4.8 \mu\text{m}$ , this result agrees with both our simulated results shown in Fig. 4(b) and that found in [15] for similar finger periodicity.

**Sensitivity Characterization:** Fig. 10 shows measured sensor sensitivity, taken by integrating the entire laser pulse by posi-

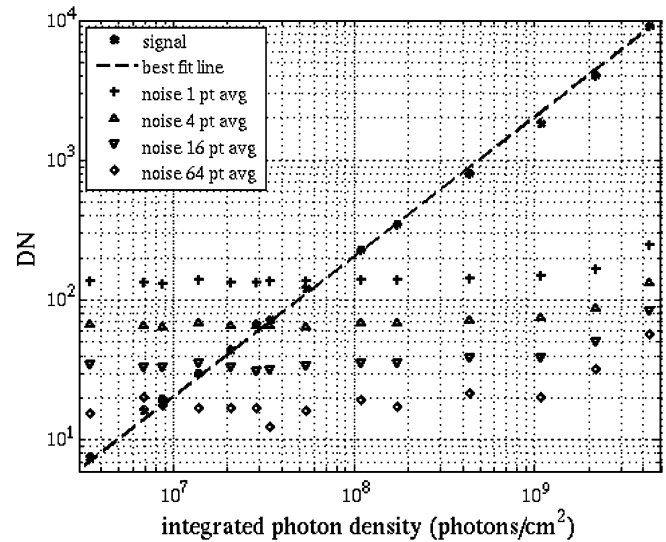


Fig. 10. Measured sensor system sensitivity.

tioning the reset turnoff before the laser pulse. Neutral density filters are added to vary the intensity of the laser signal. The noise floors are shown for different amounts of averaging. Simulation predicts a reset-noise-limited sensitivity of approximately  $188 e^-$  without any averaging, which corresponds to a photon density of  $7.3 \times 10^7$  photons/cm<sup>2</sup>, assuming 45% quantum efficiency. Measured noise floors determine a sensitivity of approximately  $7.0 \times 10^7$  photons/cm<sup>2</sup> (SNR of 0 dB) without averaging, which is within 10% of the simulated results. Measurements also show 64-point averaging improves this sensitivity by a factor of eight, as expected, to  $21.3 e^-$  or  $8.8 \times 10^6$  photons/cm<sup>2</sup>.

### B. Applications

Preliminary results are presented using the array in two applications, as an active substrate for microarray applications and



TABLE III  
OLIGONUCLEOTIDE SEQUENCES USED IN ACTIVE MICROARRAY EXPERIMENTS

Label	Sequence
Probe	5'-CTGAACGGTAGCATCTTGAC-3'
Target1	5'-GTCAAGATGCTACCGTTCAG-3'
Target2	5'-CAATACTTCGGTGGCATGAC-3'

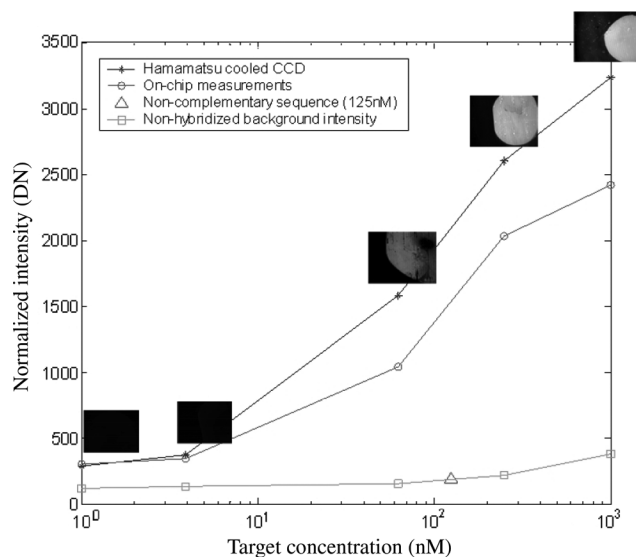


Fig. 11. Measured DNA hybridization for various target concentrations.

as a FLIM imager in epi-fluorescent microscopy. In the former case, fluorescent labels are directly immobilized on the chip surface. Time-gating is relied upon to achieve the required SBR. In the later case, the imager acts as a camera and relies on the optics of the microscope for image acquisition. Filter cubes are employed for additional background rejection.

**Microarray Measurements:** The chips are packed in ball-grid packages which are “doughnut” epoxy encapsulated, providing access to the sensor area while protecting the bond wires. The chip surface is cleaned and epoxy-derivatized with 3-glycidoxypolytrimethoxysilane. Aminated DNA probes with a length of 21 nucleotides are immobilized on top of the detector area through contact-pin spotting. DNA hybridizations are carried out with analyte solutions containing different concentrations of matching DNA (target 1) strands, which are end-labeled with biotin molecules. Hybridizations with non-complementary (target 2) sequences are also carried out as a control. Probe and target sequences are given in Table III. After hybridization, streptavidin-conjugated Qdot-655 (Invitrogen) solution is used to label and quantify the amount of hybridization and thus the concentration of matching target DNA molecules in the original analyte solution. Data from on-chip detection is verified by also imaging the chip surface in an epi-fluorescence microscope with a Hamamatsu cooled CCD imager and 500 nm long-pass filter cube. The results from different target concentrations in the hybridization analyte solutions are shown in Fig. 11, and show correlation between chip and CCD measurements. Hybridization sensitivity is primarily limited by non-specific binding of either target DNA molecules or fluorescent labels to the substrate surface, rather than the sensitivity of the sensor.

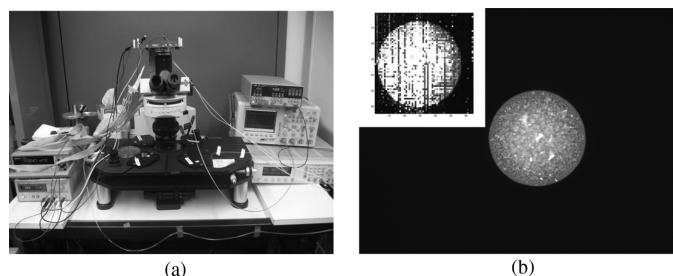


Fig. 12. Images of a fluorescent spot taken on a microscope. (a) Setup of imager on fluorescence microscope (b); images taken by chip (upper left) and CCD camera (center).

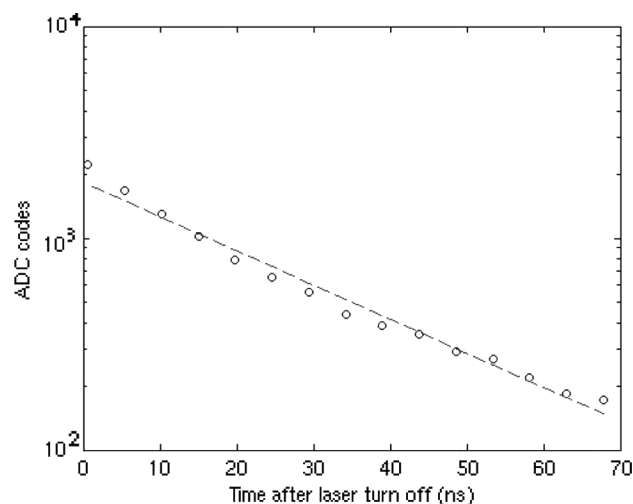


Fig. 13. Measured fluorescence lifetime of Qdot-655.

**Lifetime Imaging Application:** This chip can also function as a fluorescence lifetime imager when it is attached to the standard c-mount camera port of an Olympus BX51W1 fluorescence microscope as shown in Fig. 12(a). Using an integration period of 16 ms, a fluorescence image of an immobilized spot of Qdot-655, conjugated with streptavidin on top of epoxy-derivatized glass, is taken with the chip and shown in the insert of Fig. 12(b). The same fluorescent spot is also taken with a Hamamatsu ORCA-ER cooled CCD camera using the same exposure time, and shown in the same figure for comparison. A 10X objective lens is used and the diameter of the fluorescent spot is estimated to be 300  $\mu\text{m}$ . The surface coverage of Qdot-655 is estimated to be  $3.2 \times 10^{13} \text{ cm}^{-2}$ . Fig. 13 shows a measured lifetime response at a single pixel. This measurement shows this particular fluorophore exhibits a lifetime of 19.6 ns.

## VI. CONCLUSION

In this paper, we have described the implementation of a CMOS imager specifically designed for fluorescence lifetime imaging through a time-gated differential pixel design. These pixels possess an impulse response of less than 800 ps through an optically differential photodiode. The array has a measured sensitivity of 21.3 e-/pixel with 64-pt averaging. Future work involves demonstrating the imager in a high frame rate FLIM application as well as demonstrating an active microarray application of gene expression profiling with clinical samples.

Demonstration of the device, as an active substrate in fluorescence-based surface bioassay detecting genetic material from physiological samples, will be reported in a biotechnology journal.

#### ACKNOWLEDGMENT

The authors would like to thank UMC for chip fabrication.

#### REFERENCES

- [1] M. Schena *et al.*, "Microarrays: Biotechnology's discovery platform for functional genomics," *Trends Biotechnology*, vol. 16, pp. 301–316, Jul. 1998.
- [2] R. Sekar and A. Periasamy, "Fluorescence resonance energy transfer (FRET) microscopy imaging of live cell protein localizations," *J. Cell. Biology*, vol. 160, no. 5, pp. 629–633, Mar. 2003.
- [3] S. Draghici, P. Khatri, A. C. Ehrlund, and Z. Szallasi, "Reliability and reproducibility issues in DNA microarray measurements," *Trends in Genetics*, vol. 22, no. 2, pp. 101–109, Feb. 2006.
- [4] Y. Chen, J. Mills, and A. Periasamy, "Protein localization in living cells and tissues using FRET and FLIM," *Differentiation*, vol. 71, no. 9–10, pp. 528–541, Dec. 2003.
- [5] P. I. H. Bastiaens and A. Squire, "Fluorescence lifetime imaging microscopy: Spatial resolution of biochemical processes in the cell," *Trends Cell Biology*, vol. 9, pp. 58–52, Feb. 1999.
- [6] X. Michalet *et al.*, "Quantum Dots for living cells, *in vivo* imaging, and diagnostics," *Science*, vol. 307, pp. 538–544, Jan. 2005.
- [7] R. A. Yotter and D. M. Wilson, "A review of photodetectors for sensing light-emitting reporters in biological systems," *IEEE Sensors J.*, vol. 3, no. 3, pp. 288–303, Jun. 2003.
- [8] W. Becker *et al.*, "Fluorescence lifetime imaging by time-correlated single-photon counting," *Microscopy Research and Techniques*, vol. 63, pp. 58–66, 2004.
- [9] A. C. Mitchell, J. E. Wall, J. G. Murray, and C. G. Morgan, "Direct modulation of the effective sensitivity of a CCD detector: A new approach to time-resolved fluorescence imaging," *J. Microscopy*, vol. 206, pt. 3, pp. 225–232, Jan. 2002.
- [10] A. V. Agronskaia, L. Tertoolen, and H. C. Gerritsen, "Fast fluorescence lifetime imaging of calcium in living cells," *Journal of Biomedical Optics*, vol. 9, pp. 1230–1237, Nov. 2004.
- [11] G. Patounakis, K. L. Shepard, and R. Levicky, "Active CMOS array sensor for time-resolved fluorescence detection," *IEEE JSSC*, vol. 41, no. 11, pp. 2521–2530, Nov. 2006.
- [12] T. Huang, S. Sorgenfrei, K. L. Shepard, P. Gong, and R. Levicky, "A CMOS array sensor for sub-800-ps time-resolved fluorescence detection," in *IEEE CICC*, Sep. 2007, pp. 829–832.
- [13] D. Sander *et al.*, "Low-noise CMOS fluorescence sensor," in *IEEE ISCAS*, May 2007.
- [14] H. Eltoukhy, K. Salama, and A. El Gamal, "A 0.18  $\mu\text{m}$  CMOS bioluminescence detection lab-on-chip," *IEEE JSSC*, vol. 41, no. 3, pp. 651–662, Mar. 2006.
- [15] J. Genoe *et al.*, "Calculation of the current response of the spatially modulated light CMOS detector," *IEEE Trans. Electron Devices*, vol. 48, no. 9, pp. 1891–1902, Nov. 2004.
- [16] H. Tian, B. Fowler, and A. El Gamal, "Analysis of temporal noise in CMOS photodiode active pixel sensor," *IEEE JSSC*, vol. 36, no. 1, pp. 92–101, Jan. 2001.
- [17] B. Fowler, M. D. Godfrey, J. Balicki, and J. Canfield, "Low noise readout using active reset for CMOS APS," in *Proc. SPIE*, May 2000, vol. 3965, pp. 126–135.
- [18] L. J. Kozlowski *et al.*, "Pixel noise suppression via SoC management of tapered reset in a  $1920 \times 1080$  CMOS image sensor," *IEEE JSSC*, vol. 40, no. 12, pp. 2766–2776, Dec. 2005.
- [19] J. Yang *et al.*, "A 3 Mpixel low-noise flexible architecture CMOS image sensor," in *ISSCC Dig. Tech. Papers*, Feb. 2006, pp. 496–497.
- [20] S. J. Daubert, D. Vallancourt, and Y. P. Tsvividis, "Current copier cells," *Electron. Lett.*, vol. 24, pp. 1560–1562, Oct. 1988.
- [21] S. J. Daubert and D. Vallancourt, "A transistor-only current-mode  $\Sigma\Delta$  modulator," *IEEE JSSC*, vol. 27, no. 5, pp. 821–830, May 1992.
- [22] R. van de Plassche, *Analog-to-Digital and Digital-to-Analog Converters*. New York: Springer, 1994.



**Ta-chien D. Huang** received the B.S. degree in electrical engineering from Columbia University, New York, NY, in 1997 and the M.S. degree in electrical engineering from Stanford University, Stanford, CA, in 1999. From 1999 to 2003, he was a member of technical staff with Sun Microsystems Inc., Vello Communications Inc., and Netlogic Microsystems Inc., designing high speed I/O and mixed-signal integrated circuits. Since 2003, he has been pursuing the Ph.D. degree in electrical engineering at Columbia University. His research interests include integrated circuit design for biosensing applications, computational systems biology, and high performance analog/mixed-signal integrated circuit design.

Mr. Huang received the Myril B. Reed Best Paper Award of the 49th MWSCAS in 2007.



**Sebastian Sorgenfrei** received the B.A. degree in physics from Williams College, Williamstown, MA, in 2005, and the B.S. and M.S. degrees in electrical engineering from Columbia University, New York, NY, in 2005 and 2006, respectively. Since 2006, he has been pursuing the Ph.D. degree in electrical engineering at Columbia University.

His research interests include analog/mixed-signal integrated circuit design, carbon nanotube devices and novel interfaces for biosensor applications. He has held internship positions at Porsche AG, Infineon

Technologies AG and Robert Bosch LLC.



**Ping Gong** received the B.S. degree in chemistry from Peking University, Beijing, China in 1999 and the Ph.D. degree from Colorado State University, Fort Collins, CO, in 2006 in analytical chemistry. She has since worked as a postdoctoral research associate at Columbia University in the Departments of Chemical and Electrical Engineering. Her research interests include the development of electrochemical methods in the characterization and quantification of surface DNA hybridization behavior for biosensing applications and the development of bio-conjugation, microarray surface fabrication, characterization, and fluorescence quantum dot detection methods for integrated CMOS biosensor applications.

Dr. Gong is a member of the American Chemical Society and the American Vacuum Society.



**Rastislav Levicky** received the Ph.D. degree in chemical engineering from the University of Minnesota, Minneapolis in 1996, and the B.S. degree in chemical engineering from Columbia University, New York, NY, in 1991. His Ph.D. thesis focused on self-organized polymer assemblies at solid-liquid interfaces and in thin films.

From 1996 to 1998 he was a National Research Council Postdoctoral Associate with the National Institute of Standards and Technology (NIST) in Gaithersburg, MD, where he studied the interfacial organization and biological activity of polynucleic acids with neutron beam and optical techniques. In July 1998 he joined the Chemical Engineering faculty at Columbia University, from where he moved to the Department of Chemical and Biological Engineering at Polytechnic Institute of New York University in July 2006. His current research interests encompass biointerfacial engineering, biomolecular diagnostics, kinetics of interfacial reaction networks, and electrochemistry.

Dr. Levicky is a member of the American Institute of Chemical Engineers, the American Chemical Society, the American Physical Society, and the American Vacuum Society. He is a recipient of the National Science Foundation CAREER Award for Young Investigators, and the 2001 Distinguished Faculty Teaching Award from Columbia University Engineering Alumni Association.



**Kenneth L. Shepard** (M'91–SM'03–F'08) received the B.S.E. degree from Princeton University, Princeton, NJ, in 1987 and the M.S. and Ph.D. degrees in electrical engineering from Stanford University, Stanford, CA, in 1988 and 1992, respectively.

From 1992 to 1997, he was a Research Staff Member and Manager with the VLSI Design Department, IBM T. J. Watson Research Center, Yorktown Heights, NY, where he was responsible for the design methodology for IBM's G4 S/390 microprocessors.

Since 1997, he has been with Columbia University, New York, where he is now Professor. He also was Chief Technology Officer of CadMOS Design Technology, San Jose, CA, until its acquisition by Cadence Design Systems in 2001. His current research interests include design tools

for advanced CMOS technology, on-chip test and measurement circuitry, low-power design techniques for digital signal processing, low-power intrachip communication, and CMOS mixed-signal design for biological applications.

Dr. Shepard was Technical Program Chair and General Chair for the 2002 and 2003 International Conference on Computer Design, respectively. He has served on the Program Committees for ISSCC, VLSI Symposium, ICCAD, DAC, ISCAS, ISQED, GLS-VLSI, TAU, and ICCD. He received the Fannie and John Hertz Foundation Doctoral Thesis Prize in 1992, a National Science Foundation CAREER Award in 1998, and the 1999 Distinguished Faculty Teaching Award from the Columbia Engineering School Alumni Association. He has been an Associate Editor of IEEE TRANSACTIONS ON VERY LARGE-SCALE INTEGRATION (VLSI) SYSTEMS and is current an Associate Editor for the IEEE JOURNAL OF SOLID-STATE CIRCUITS.